Mid-wave and long-wave infrared signature model and measurement of power lines against atmospheric path radiance

Patrick Leslie,[1,*] **Orges Furxhi,**[2] **Robert Short,**[3] **Robert Grimming,**[4] **Anne Lautzenheiser,**[5] **Tex Longcor,**[5] **and Ronald Driggers**[1]

[1]*Univeristy of Arizona, Wyant College of Optical Sciences, 1600 E University Blvd, Tucson, AZ 85721, USA*
[2]*Camera Systems and Computation Imaging IMEC, 194 NeoCity Way, Kissimmee, FL 34744, USA*
[3]*Redstone Test Center, 4500 Martin Rd SW, Huntsville, AL 35808, USA*
[4]*Univsersity of Central Florida, CREOL, 4304 Scorpius St, Orlando, FL 32816, USA*
[5]*Program Office Apache, Huntsville, AL 35808, USA*
*leslieps@email.arizona.edu

Abstract: The signal to noise ratio and corresponding visibility of power cables as seen by military aircrafts is critical for crew safety. During low altitude operations, rotorcraft systems must be able to navigate these power lines during flight. Many of these military missions are flown at night which means the reflective bands including the visible, near infrared and short-wave infrared do not provide sufficient light. However, the emissive bands of the mid-wave infrared (MWIR) and long-wave infrared (LWIR) can be used to distinguish the location of these wires. LWIR sensors are typically used for pilotage applications. In both the LWIR and MWIR, the signal to noise depends on the wire emissivity and reflectivity as well as the ground and sky background path radiance. The signal to noise ratio is strongly dependent on the elevation of the viewing angle. In this paper, we model the signal to noise ratio as a function of elevation viewing angle using wire reflectivity and emissivity as well as MODTRAN calculations for path radiance. We also take MWIR and LWIR measurements to compare these two bands to the modelling results. We provide a summary of both model and measurements and make conclusions.

1. Introduction

The ability to see power cables for crew safety is vital. Out of all helicopter accidents, 5.5% of domestic accidents involved power lines between 1994 and 2002 [1]. From 1994 to 2018 there has been at least two wire strike accidents each year. While these percentages only show some of the accidents overall, the real cost involved are fatalities and damage. In the U.S. from 1994 to 2018, 33% of wire strike accidents resulted in at least one fatality and 34% of helicopters were completely destroyed with the rest sustaining heavy damage [2]. Shown with available data from 1994 to 2018, there were 214 wire strike accidents resulting in 124 fatalities due to helicopter wire strikes. Fatalities involving wires are much higher in comparison to other categories of crashes.

To combat the number of accidents and fatalities due to power lines two paths of technology developed. Wire Strike Protection Systems are a passive technology that consist of a windshield deflector and an upper and lower wire cutter to avoid entanglement [2]. These systems are relatively low cost in comparison to active vision systems but can fail due to large diameter wires, slow speeds and if the wires do not contact the helicopter near the cutters. Vision systems on the other hand give the pilot an opportunity to detect the wire and evade it. During the day visible, near infrared and short-wave infrared sensors can assist pilots to visualize obstacles during flight. However, when flying at night only the emissive bands can aid in obstacle detection. FLIR

and Lockheed-Martin both utilize the mid-wave infrared and the long-wave infrared in their electro-optical sensor systems for pilotage and targeting [3,4]. These bands range from 3-5 µm and 8-14 µm respectively and are critical for identifying objects at night.

In this paper, a mathematical model is created to incorporate sky radiance, ground radiance, wire reflectivity, wire emissivity and equivalent black body temperature (EqBB). From a radiometric point of view, this model is used to calculate the signal of the wire and the atmospheric path radiance in the MWIR and LWIR resulting in a wire contrast radiance and contrast EqBB temperature (Figs. 1(a)–1(c)). The model can predict for the two emissive bands (MWIR and LWIR) at which angle the wire is no longer be distinguishable from its background. The sky and ground radiance data for the model is provided by MODTRAN as well as experimental measurement data. The measurements taken are both of the average wire EqBB temperature and its background path radiance at each angle from 0 to 360° around the wire. The same data is taken in the LWIR and MWIR to determine the contrast of the wire to its background. Finally, the results provide for a comparison of wire contrast in the MWIR vs LWIR. The results also provide a deeper understanding of the zero contrast angles in the MWIR vs LWIR.

Fig. 1. Power Lines in the LWIR. Figure 1(a) (left) shows the wires against a cold sky where the ground reflection makes the wires bright. Figure 1(b) (middle) shows where the wire radiance matches the sky path radiance (i.e., no contrast). Figure 1(c) (right) shows a look down where the wires are dark reflecting cold sky against a warmer ground background.

2. Background

Pilotage is an act of directing the movement of a vehicle by visual electronic observations of recognizable landmarks [5]. The electronics that make the visualization of the pilots' surroundings possible are mobility sensors. These sensors follow the pilot's line of sight and collect more data from the environment than the pilot could naturally see, to make the best possible choices in operating the vehicle. One of the main uses for these sensors are nighttime operations of terrestrial or aerial vehicles to avoid objects that might not be visible by the pilot's unaided sight. Combat pilotage systems use image intensifiers and electron multiplying charge-coupled device (EMCCD) systems for low light imaging. MWIR or LWIR systems are used when there is negligible visible light. While MWIR systems have been used for pilotage, LWIR systems are much more common. The two LWIR systems used in pilotage are uncooled infrared (UCIR) and cryogenically cooled photon focal planes (e.g. either mercury-cadmium-telluride (MCT) or TypeII Superlattice). For high performance pilotage, cooled LWIR sensors are required.

For night pilotage, sensor materials that are sensitive to photons from the emissive bands were created for negligible visible light pilotage. The emissive bands collect photons from the radiation that is given off by an object's total energy. Current 3rd Generation FLIR Sensor Engines for US. Army systems incorporate both of these bands on a focal plane array [6]. The emission from these objects is determined by object emissivity and reflectivity, object temperature and ambient temperature. The implementation of these systems has proven to help in pilotage, especially at night, but metrics needed to be created to characterize how to determine if an object like a power

line is even visible. The visibility depends not only on the performance of the sensor, but also the emissivity and reflectivity of the targets, like a wire, and also the background radiometry such as ground or sky radiance.

The Snellen ratio was created as a visual acuity test and is still used as a standard today for some tasks. This ratio tests the resolution of a person's vision and can interpret the limit of an individual's sight. With 20/20 being the average of all adults, most younger people, or those with good vision score around 20/16 to 20/12 with 20/12 corresponding to an angular resolution of 0.01 degrees or 0.6 arc minutes [7]. This acuity test can then be related to a displays device pixel ratio (DPR) to determine the upper limit of a sensor needed that will give no added benefit to the pilot. The relationship between visual acuity and contrast can also be measured with high contrast charts with a sinewave pattern [8]. The contrast threshold function (CTF) for human vision can also be used to determine a sensor CTF that is directly related to pilotage performance. This is a more recent metric associated with pilotage performance as developed by Vollmerhausen and Bui [9].

When creating pilotage systems, the resolution and signal to noise ratio of the camera and the display system must be able to create a clear image for the pilot to see. The camera and display that the observer uses to visualize objects both add blur to the overall system making it more difficult to distinguish the target. When imaging with the eye, the systems CTF becomes the CTF of the eye degraded by the blur and noise of this system. The noise of the signal is introduced by the photo-detection components and the blur of the signal comes from diffraction, aberrations, sensor array size, pixel pitch, the blur of the display and blur introduced by the eye itself. Other obscurants such as glare and weather conditions can also cause degradation of the contrast as well.

For target acquisition performance, the Target Task Performance (TTP) metric was created to quantify the quality of an image as a weighted integral over the spatial frequency of the ratio between signal and CTF. This metric can give a good representation of both well-sampled and under-sampled imagers and can predict the performance impact of frequency boost, colored noise, and other characteristics of modern images [9]. The TTP metric was later modified to provide estimates of pilotage performance. While the pilotage performance model relates the pilot's ability to maneuver the aircraft with various background contrast levels, it was never modified to predict the visibility of wires.

Pilotage is not the only industry that is interested in the visualization of power lines. Companies that build and manage the power lines use UAVs (unmanned aerial vehicle) for thermology to map potential system failures. These UAVs utilize automatic target detection software as well as both infrared and visible sensors to detect faults in wires, insulators, and other hardware [10]. Examples of these could be broken or rusted insulator chains, frayed or detached wires and rusted or broken attachment points. These faults can be identified from both the visual and infrared sensors on the UAV. The focus of the infrared sensors for power equipment thermology mapping is to detect spikes in temperatures of the power lines or other equipment which usually corresponds to a problem in the system.

3. Mathematical model

The model that we develop is intended to implement measured and simulated atmospheres to predict the contrast between the average EqBB temperature of a wire and its background. To keep things simple, a wire perpendicular to the optical axis is considered. There is no tilt or sag of the wire for this model. The first step of the model is to match the field of view (FOV) and mainly the line of sight (LOS) of the scene in the LWIR and MWIR. At each angle from 0° (looking at the horizon) to 360°, the sky and ground radiance are measured, or simulated, and can be converted into EqBB temperature (Fig. 2). These values are then used to both model the average EqBB temperature of the wire as well as the contrast of the wire to its background.
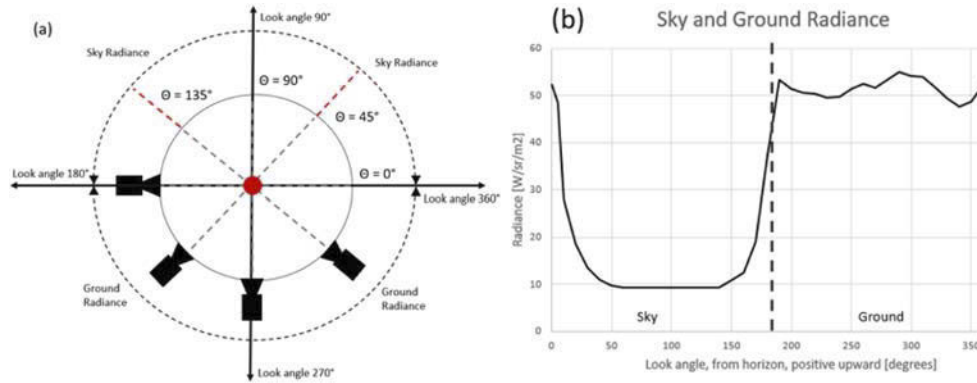
Fig. 2. (a) Diagram of the orientation of the sensor when measuring the sky and ground radiance. As the sensor decreases in height around the center axis the angle increases. (b) LWIR sensor data of the sky radiance starting at the horizon and increasing in look angle. The dotted line in the middle is drawn at 180° Separating the sky radiance (left) and ground radiance (right). The measurements do not exceed 9.315 W/sr/m^2 (appx. -60°C) due to the limitations of the camera.

A multi-faceted surface shown in Fig. 3, or "wire," is implemented in the center of the scene so that one pixel of the sensor can resolve the wire (i.e., a single detector angular subtense matches the dimension of diameter of the wire). Each facet of the wire reflects its corresponding sky or ground radiance for each angle around the wire. The radiance corresponding to the facet of each wire integrates resulting in an average wire EqBB temperature at each angle. The effective surface area of each facet of the wire as seen by the sensor is given as,

$$A_{EFF} = \mathbf{Ldcos(\alpha)} \qquad [\text{cm}^2] \qquad (1)$$

where L is the length of the wire, d is the constant width of each facet that is sometimes limited by the azimuth detector angular subtense, $dcos(\alpha)$ is the width of a faceted segment from the point of view of the pixel and α is the angle at which that facet is tilted as seen by the sensor (Fig. 3). For this model, it is assumed that the distance between the detector and the wire is substantially large enough to state that the sky and ground radiance as seen by the detector is two times the angle of the facet.

The second step is to take the corresponding area radiance from the wire that is viewed by the sensor and integrate (sum) the intensity reflected from the wire. This integrates all of the wire facet radiances that are seen by the sensor and gives an overall intensity of the wire. This approach assuming a specular facet is provided by,

$$I_{REF} = \sum_{\alpha=\alpha_1}^{\alpha_n} \rho L_{ATM}(\theta = 2\alpha)\mathbf{Ldcos(\alpha)} \qquad [\text{watts/sr}] \qquad (2)$$

$$I_{REF} = \sum_{\alpha} \rho L_{ATM}(2\alpha)\mathbf{Ldcos(\alpha)} \qquad [\text{watts/sr}] \qquad (3)$$

where ρ is wire reflectivity, L_{ATM} is the radiance of the atmosphere [W/cm^2-sr], I_{REF} is the intensity [W/sr] and θ is the reflected atmosphere angle [deg]. The result of this summation is converted to the average EqBB temperature that is reflected off the wire and viewed by the sensor at the different sensor angles. Next the emission (as opposed to reflection) from the wire at each
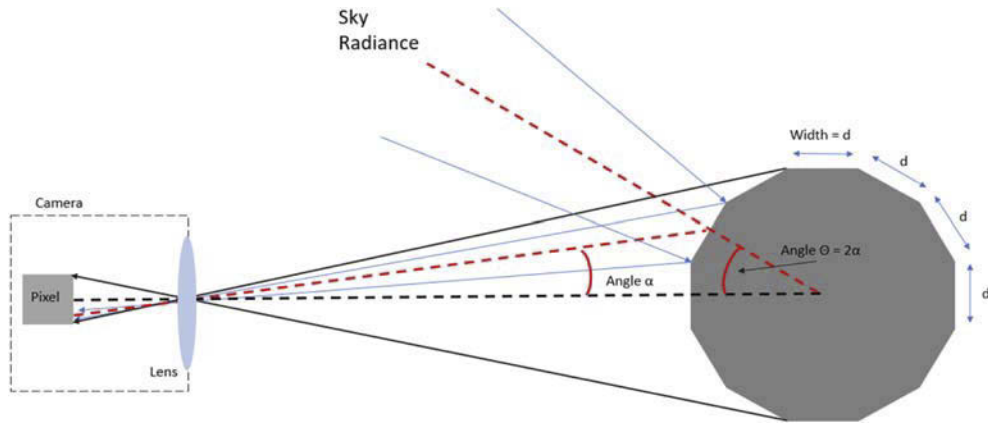
Fig. 3. The faceted surface on the right is a simple representation of the modeled wire. The IFOV of the pixel is filled with the entire signal given by the wire. The area of each facet incorporated different portions of the sky and ground radiance that all average to give a single value on the detector. The angle that is reflected from the facet (θ) is two times the angle that the facet is to the direction of the sensor (α). Each of the facet faces are constant (d). Diffraction is ignored in the model.

facet needs to be incorporated. The intensity from emission is,

$$I_{EM} = \in L_{BBWire}Ldcos(\alpha) \qquad [\text{watts/sr}] \qquad (4)$$

where $\in$ is wire emissivity and L_{BBWire} is the EqBB temperature of the wire. The L_{BBWire} provides a Lambertian emissive. To find the total intensity of the wire the two equations are added.

$$I_{TOT} = \sum_{\alpha}\{\rho L_{ATM}(2\alpha)Ldcos(\alpha)+ \in L_{BBWire}Ldcos(\alpha)\} \qquad [\text{watts/sr}] \qquad (5)$$

An assumption is made that the wire is a far distance from the detector that is collecting its signature on a single pixel. Then with small angle, α's (in radians) the facet can be written as $r_{WIRE}(d\alpha)$. The intensity is then given by

$$I_{TOT} = \sum_{\alpha}\{\rho L_{ATM}(2\alpha)Lcos(\alpha)r_{WIRE}d\alpha+ \in L_{BBWire}Lcos(\alpha)r_{WIRE}(d\alpha)\} \; [\text{watts/sr}] \quad (6)$$

An integral is then created to summate the total intensity given by all facets of the wire,

$$I_{TOT} = \int_{\alpha=\frac{-\pi}{2}}^{\alpha=\frac{\pi}{2}} [\rho L_{ATM}(2\alpha)+ \in L_{BBWire}]Lr_{WIRE}cos(\alpha)d\alpha \quad [\text{watts/sr}] \qquad (7)$$

Equation (7) assumes the reflected portion of the wire is specular. The reflected light is a condition of specular and Lambertian, or a bidirectional reflectance distribution function (BRDF) can be used. For the reflected component, $\rho L_{ATM}(2\alpha)$, a portion β is specular and a portion (1-β) is Lambertian. So, the overall equation that includes reflection and emission as well as specular and Lambertian components of the reflected component is,

$$I_{TOT} = \int_{\frac{-\pi}{2}}^{\frac{\pi}{2}} \left\{\rho\left[\beta L_{ATM}(2\alpha) + \frac{1-\beta}{2}\int_{2\alpha-\frac{\pi}{2}}^{2\alpha+\frac{\pi}{2}} cos(\theta)L_{ATM}(\theta-2\alpha)d\theta\right] + \in L_{BBWire}\right\}$$
$$\times Lr_{WIRE}cos(\alpha)d\alpha \qquad (8)$$

The total intensity given fills the pixel of the sensor. The limit of the integral is spatially limited to a specified IFOV. This limit is given by the half of the wire the sensor can see from one

side, which we limit as -π/2 to π/2. The power, in watts, on the IFOV of the detector is

$$P_{pixel} = I_{TOT} \frac{A_{sensor\ aperture}}{R^2} \qquad [watts] \qquad (9)$$

where P is the power on the single pixel, A is the area of the sensor aperture [cm^2] and R is the distance from the sensor to the wire. This result is then graphed, comparing the average power on a pixel of the wire at each angle from 0-360° around the wire. Lastly the average EqBB temperature of the wire is subtracted from the EqBB temperature of the measured or simulated background at that same angle to compare the contrast of the two at each angle. Contrast can be provided in either radiance or e EqBB temperature (which is a radiometric quantity).

4.　Wire measurements

A high voltage power line was cut at approximately one meter in length and used to take images for the average wire EqBB temperature data collection. The sensors used in this study were a FLIR T1020sc with a 28° FOV in the LWIR and a Telops M150 Spark with a 20° FOV in the MWIR. The measurements were taken after the sun had set to avoid any solar reflections that would be present in the 3-5 µm range of our MWIR sensor. Solar loading of the atmosphere and reflections in that band does change the contrast of the wire as well as the path radiance of the sky and ground, particularly in the MWIR. To measure the wire at a constant distance and to avoid any thermal radiation from the sensor operator, an apparatus was made to hold the camera at all 0 - 360° angles around the wire (Fig. 4). By using an inclinometer on the arm of the apparatus that holds the sensor, each angle could be specifically set for increments of 10°. The length of the arm was made so the wire could be easily resolved by the camera as well as have sufficient of background radiance data.

Fig. 4. Apparatus which holds the either the LWIR sensor or MWIR sensor (pictured) which contains the wire in the middle of the rotational axis, an arm holding a sensor at a constant distance, an inclinometer on the arm and a large disc to clamp the arm in place.

Starting with the sensor looking at the horizon (0°) and decreasing the angle of the arm the bottom of the wire and the sky background radiance was measured first from angles 0 - 180°. This was followed by the top of the wire and the ground background radiance from 190 - 350°. To obtain the background path radiance, the EqBB temperature of the sky and ground was taken at each of these angles in the middle of the FOV (next to the wire) for both the MWIR and LWIR sensors (Fig. 5).

At these same angles, the average wire EqBB temperature was recorded. The wire and background were clearly identified and integrated using the pixels on the wire and the background pixels near the wire. The integrated intensity of the wire was converted to a wire EqBB temperature for all angles from 0-360° in both the MWIR and the LWIR (Fig. 6).
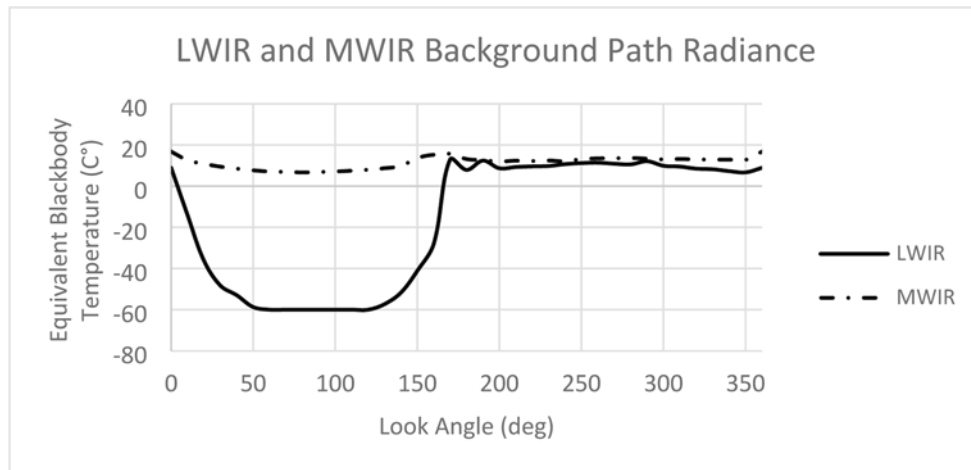
Fig. 5. The measured sky and ground path radiance in both the MWIR and the LWIR. The LWIR EqBB temperature dramatically decreases as the sensor look angle increases towards the sky. The change in EqBB temperature for the MWIR cameras is much less. Again, the measurements do not exceed at -60C due to limitation of the LWIR camera.
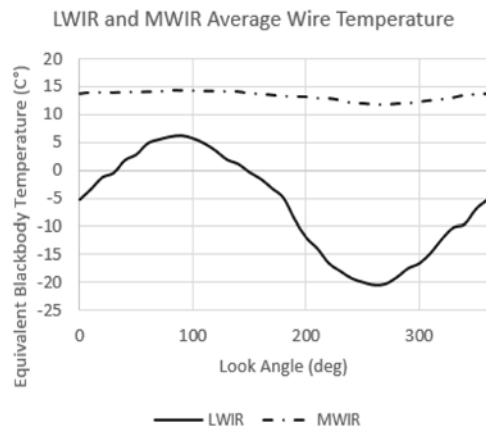
Fig. 6. (Left): The LWIR and MWIR wire averages also have a large difference in their change in EqBB temperature. However, both of their positive and negative peaks happen when looking at the top and the bottom of the wire respectively (90° and 270°).

The increase in wire EqBB temperature while the camera was pointed towards the sky was due to the bottom of the wire reflecting the warm ground. Similarly, the decrease in EqBB temperature while the camera was pointed towards the ground was due to the top of the wire reflecting the cold sky. The vast different in fluctuation between the MWIR and the LWIR wire averages is attributed to their measured background. The steep difference in the background of the LWIR is easily seen from the wire averages from Fig. 6 as well as the much smaller change in the MWIR from its background measurements. This fact results in a lower contrast between the background and the averaged wire for the MWIR than it does for the LWIR (Fig. 7). By taking the differences between the background and the wire averages, the contrast between the two can be quantized. When the contrast is zero, the wire is indistinguishable from the background and as the angle increases or decreases from the axis, the contrast increases. In both cases the contrast reaches zero around the horizon but not at the same angle for the two bands.
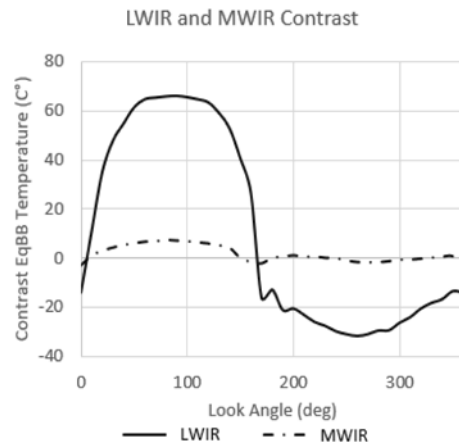
Fig. 7. (**Right**): LWIR and MWIR contrast between the average wire EqBB temperature and the background path radiance. The contrast plotted relates to the probability of identifying the wire in its scene. The greater the distance from the x-axis, the more contrast, therefore a higher likelihood of detection.

5. Model results with measured sky radiance

To validate the simple model, the measured wire average EqBB temperature and background EqBB temperatures are linearly interpolated to two-degree increments. The limited radiance of the atmosphere in the LWIR was also interpolated to better match the average wire EqBB temperature. These temperatures are plotted with their corresponding angle from 0° to 360° to compare the modeled average wire EqBB temperature. The background EqBB temperatures of the atmosphere and ground are inserted into the model. Both the specular and Lambertian individual models are tested with varying emissivity to compare their results to the measured wire EqBB temperature (Fig. 8).

The specular model closely matches the amplitude of the measured wire, but its total average EqBB temperature is lower than the measured data. The increased emissivity causes a reduction in the wires amplitude and increased the total wire average EqBB temperature. For the Lambertian model, the amplitude of the simulated wire EqBB temperature is larger compared to the wire EqBB temperature. Similarly, to the specular case, when the emissivity is increased the amplitude decreases but the average EqBB temperature is much higher.

By combining the specular and Lambertian models into one, the ratio of the Lambertian and specular model is linearly tuned by taking a percentage of each and adding the two cases together as described by Eq. (8). This phenomenon coincides with the bidirectional reflectance distribution function (BRDF) which characterizes materials through specular and diffuse reflectance measurements [11]. Most natural surfaces are neither 100% specular or Lambertian and generally are a combination of the two. There are different models to incorporate BRDF into measurements using complex functions but for this model a simple linear combination is used. In addition of the ratio of contribution from the two models, the emissivity is adjusted to match the amplitude of the measured wire average EqBB temperature.

In both the MWIR and LWIR cases the ratio and emissivity are tuned for two different measurements cases to ensure validity of the model and measurement (Fig. 9). The emissivity's that allowed for the accurate validation of these models coincide with an emissivity of non-weathered aluminum. The measured emissivity's of unoxidized aluminum by thermal imager is around 0.1 [12]. The conductor used in the outer portion of high voltage power lines is aluminum with a steel core for strength [13].
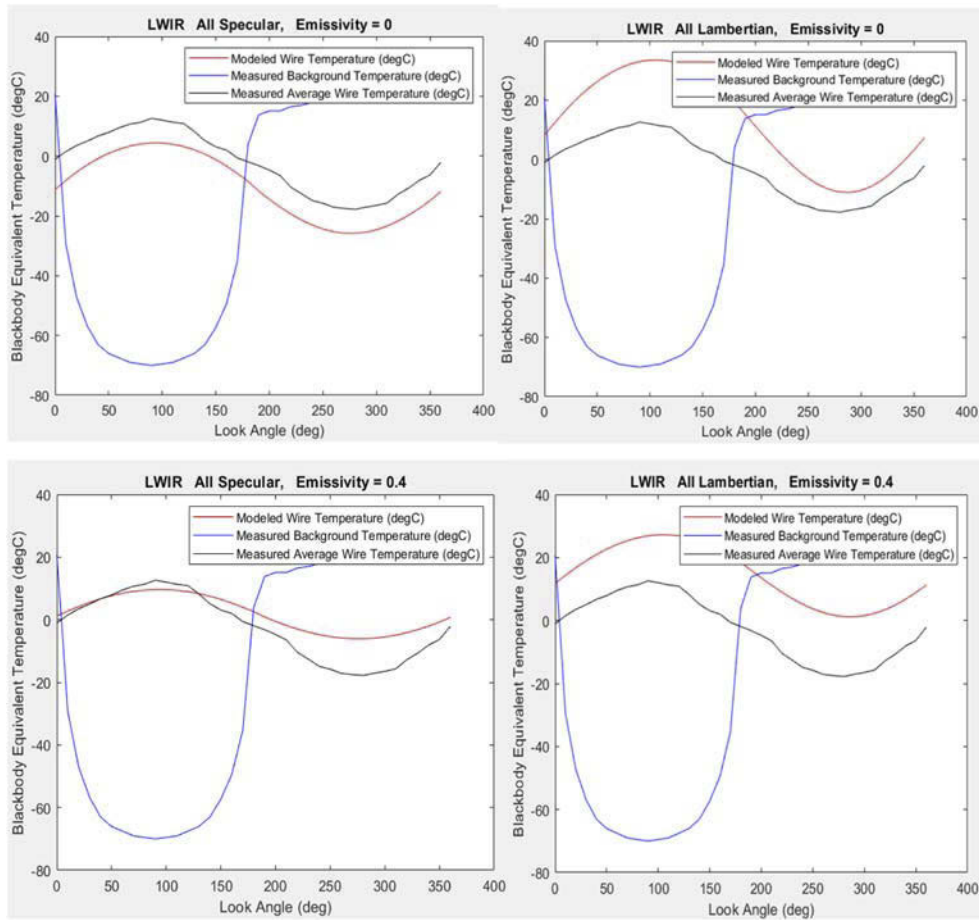
Fig. 8. The four cases show the effects of the emissivity changes from 0 to 0.4. For these cases only specular or only Lambertian models were run with the respective emissivity's.

The BRDF model and emissivity of the aluminum wire for the LWIR accurately predicted the measured wire EqBB temperatures. Both the amplitude and average wire EqBB temperatures for all 360° were accurately predicted based on the combination model. The difference of emissivity's and the BRDF ratio between the two cases were reasonable and matched public data on wire surfaces. The model for the MWIR is harder to match due to its reflectivity and sensitivity but the best match was achieved as seen in Fig. 9. The wire measurements were taken at night to avoid major reflectivity readings that occur during the day in the MWIR but there can still be effects from the surroundings. The MWIR model does give a closely matched wire average EqBB temperature.
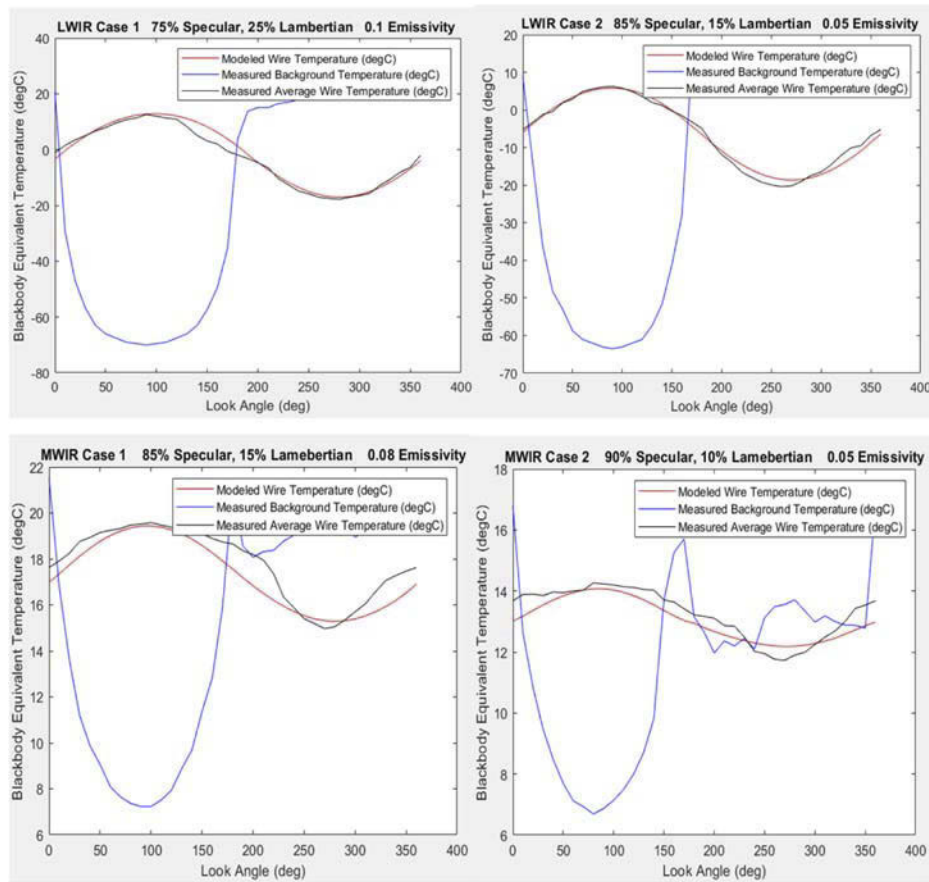
Fig. 9. The measured and modeled wire average EqBB temperatures are plotted with their corresponding background EqBB temperatures. Case 1 and Case 2 measurements were taken on two different days after the sun had set to avoid large variation in the MWIR. The MWIR and LWIR data were taken at the same time during the measurements.

6. Model results with Artic, U.S. standard, and tropical atmospheres

After the validation of the combined models with the LWIR and MWIR measurements, the model was used to predict the wire average EqBB temperatures in the MWIR and LWIR bands for other atmospheres. To avoid travelling all over the world to collect a variety of atmospheric data, MODTRAN generated atmospheres were used to generate the background path radiance used in the BRDF model. The model used the MODTRAN atmospheres to simulate the average wire EqBB temperature for all 360° and the contrast of the generated atmosphere and its associated wire. Six cases were modeled based on a few of the standard atmospheres that MODTRAN exports. U.S. Standard, Tropical and Artic path radiance were generated in both the LWIR and MWIR bands for a variety of concentration of aerosols and ground temperatures. The contrast of the MODTRAN background and the modeled wire EqBB temperatures were given for each band (Fig. 10). An average ratio and emissivity for the BRDF model was used based on the two cases shown from Fig. 9. The ratio for all cases was 80% specular and 20% Lambertian with an emissivity of 0.1.

The amount of contrast for each of the modeled atmospheres is significantly less in the MWIR than the LWIR. This was also seen in the measurements taken of the wire with the MWIR and
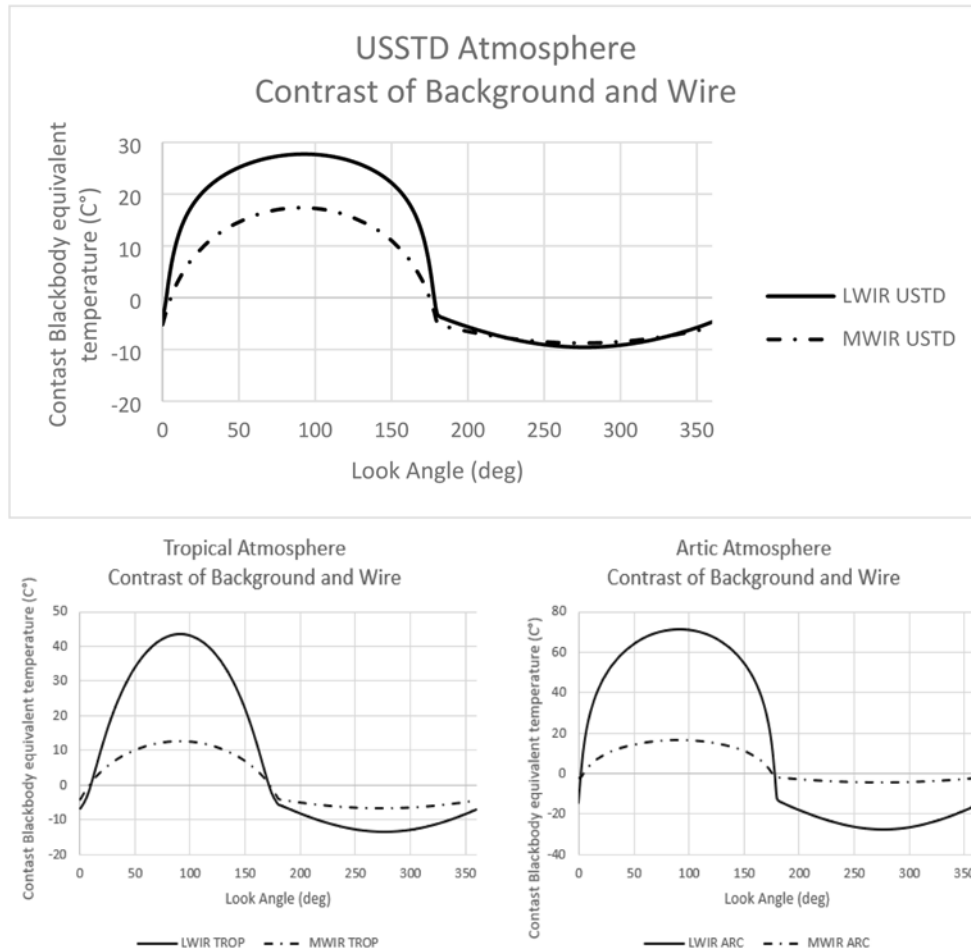
Fig. 10. LWIR and MWIR contrast between the MODTRAN generated atmospheres and the simulated average wire EqBB temperature given by the BRDF model.

Table 1. The angle at which the contrast in both the LWIR and MWIR goes to zero is seen to be different for every case in the modeled and measured atmospheres. The amount of contrast that the other band sees when the other is at zero is recorded and shown as well. The lowest contrast that would be always seen by a dual band wire detection system would be -0.67 ℃.

Atmosphere	Zero Contrast Look Angle LWIR (In degrees)	Zero Contrast Look Angle MWIR (In degrees)	MWIR contrast when LWIR equals zero (EqBB Temp in Degrees C)	MWIR contrast when LWIR equals zero (EqBB Temp in Degrees C)
US Standard	4.6 & 175.4	5.5 & 174.5	-0.75°C	-5.83°C
Tropical	9.5 & 171.5	8.0 & 172.0	-0.67°C	-1.7°C
Artic	2.3 & 176.7	4.4 & 175.6	-2.4°C	11°C

LWIR sensors (Fig. 7). Another important observation is that for each of the three atmospheres, the LWIR and MWIR contrast goes to zero at different look angles (Table 1). When the contrast is zero for one band, the EqBB temperature between the background and the wire in the other band is not. The angles for the two bands where the contrast goes to zero is recorded in Table 1.

The lower of the two numbers would represent the minimum contrast that a dual band pilotage system for wire detection would always have on the wire in that environment.

7. Discussion

For high power voltage line detection, the larger the contrast between the wire and the background, the higher probability there is for detection. For the MWIR and LWIR sensors, the LWIR provides significantly more contrast in all scenarios measured and modeled as seen in Figs. 7 and 9. The performance of the two bands is compared by the contrast in the LWIR vs the contrast in the MWIR for all modeled and measured scenarios (Fig. 11). When the x-axis is crossed, this is when the contrast in the LWIR is zero and when the y-axis is cross this is when the MWIR is zero. Figure 11 also shows well again that there is no atmosphere in this paper where the contrast is zero at the same time. Figure 11 shows a 2 to 4 times higher contrast in the LWIR versus the MWIR depending on the atmospheric conditions. Also seen, is that when the MWIR sensor is looking down from above, the contrast of the ground and the wire can be zero at various angles besides just at the horizon, where the LWIR only has the two crossing points coinciding with the horizon.
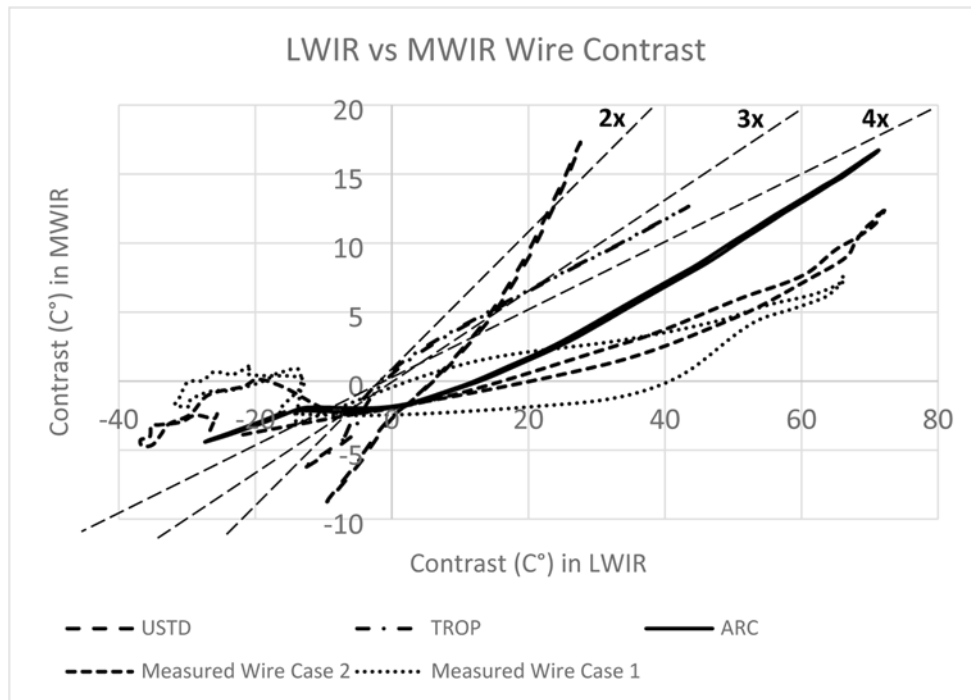
Fig. 11. This graph plots LWIR contrast vs MWIR contrast to show the two to four times better performance given by the LWIR. MODTRAN atmospheres are very symmetric showing a small gap where the measured atmospheres have different contrast giving different crossing points.

8. Conclusions and future work

Single band wire detection in pilotage is most effective with a LWIR sensor. The contrast that is achieved can be four times higher than that of the MWIR. The fact that in the MWIR the contrast

when looking down at the wire could also be zero depending on your background would make the MWIR an unreliable band for a single band pilotage system.

The contrast angle in the MWIR and LWIR is zero when viewing the wire near the horizon angle for all modelled and measured cases. Since the contrast for each band does not reach zero at the same angle, a dual band wire detection system could be beneficial for wire visibility. Based on Table 1, there could be at least a half a degree of contrast for a dual band imager, and this increases the probability of never losing sight of the wire. Future work will determine how much contrast is needed it implement two bands on the same detection system and if the small contrast gain is enough to warrant the extra cost of the dual band sensor.

Future work for wire detection systems is to introduce new environmental factors and real-world scenarios. New environmental factors will be including cloud cover and the effects on path radiance, contrast, and average wire EqBB temperature. Daytime wire detection will also be studied as a separate case due to the reflectivity in the MWIR, solar loading of the sky and sun position effects. Other effects to study, that a pilotage system would encounter in the real world, are phasing effects of the wire sagging between the poles and when the wire becomes resolved versus unresolved due to distance.

Disclosures. There are no disclosures or conflicts of interest in this work.

Data availability. Data underlying the results presented in this paper are not publicly available at this time but may be obtained from the authors upon reasonable request.

References

1. Nagaraj and T. Vengalattore, "Safety Study of Wire Strike Devices Installed on Civil and Military Helicopters," *Google Books*, Office of Aviation Research and Development, Federal Aviation Administration, Sept. 2008.
2. R. Chandrasekaran, A.P. Payan, K.B. Collins, and D.N. Mavris, "Helicopter wire strike protection and prevention devices: review, challenges, and recommendations," Aero. Sci. Technol. **98**, 105665 (2020).
3. Donald F. King, Jason S. Graham, Adam M. Kennedy, Richard N. Mullins, Jeffrey C. McQuitty, William A. Radford, Thomas J. Kostrzewa, Elizabeth A. Patten, Thomas F. McEwan, James G. Vodicka, and John J. Wootan, "3rd-generation MW/LWIR sensor engine for advanced tactical systems," *Proc. SPIE 6940, Infrared Technology and Applications XXXIV*, 69402R (22 April 2008).
4. Arnold C. Goldberg, Theodore Fischer, Stephen W. Kennerly, Samuel C. H. Wang, Mani Sundaram, Parvez N. Uppal, Michael L. Winn, Gregory L. Milne, and Mark A. Stevens, "Dual-band QWIP MWIR/LWIR focal plane array test results," *Proc. SPIE 4028, Infrared Detectors and Focal Plane Arrays VI*, (17 July 2000).
5. Richard H. Vollmerhausen, "Design criteria for helicopter night pilotage sensors," *Proc. SPIE 2075, Passive Sensors, 20750Q* (29 January 1992).
6. Antoni Rogalski and K. Chrzanowski, "Infrared Devices And Techniques (Revision)," Metrology and Measurement Systems. **21**(4), 565–618 (2014).
7. John M. Evans LLC, "Standards of Visual Acuity," Intelligent Systems Division, National Institude for Standards and Technology (June 15, 2006). https://www.nist.gov/system/files/documents/el/isd/ks/Visual_Acuity_Standards_1.pdf
8. Peter G. J. Barten, *Contrast Sensitivity of the Human Eye and Its Effects on Image Quality*. Bellingham, Wash.: SPIE Optical Engineering, 1999. PM72. Web.
9. Richard H. Vollmerhausen and Trang Bui, "Using a targeting metric to predict the utility of an EO imager as a pilotage aid," Proc. SPIE 6207, Infrared Imaging Systems: Design, Analysis, Modeling, and Testing XVII, 62070C (15 May 2006); https://doi-org.ezproxy3.library.arizona.edu/10.1117/12.668436
10. Bushra Jalil, Giuseppe Riccardo Leone, Massimo Martinelli, Davide Moroni, Maria Antonietta Pascali, and Andrea Berton, "Fault Detection in Power Equipment via an Unmanned Aerial System Using Multi Modal Data," Sensors **19**, 13 (2019).
11. Wenzel Jakob, Matt Pharr, and Greg Humphreys, *Physically Based Rendering: From Theory to Implementation*, Elsevier Science, Netherlands 2016, Federal Aviation Administration, Sept. 2008.
12. Milan Zeljković, Zorana Lanc, Branko Strbac, Aleksandar Zivkovic, Drstvenšek Igor, and Miodrag Hadžistević, "The determination of the emissivity of aluminum alloy AW 6082 using infrared thermography," Journal of Production Engineering. **18**, 23–26 (2015).
13. Mariesa L. Crow and Nirup Shetty, "Electric Power Measurements and Variables," Cutler J. Cleveland, (ed.), *Encyclopedia of Energy*, Elsevier, 2004, Pages 245-254, ISBN 9780121764807, https://doi.org/10.1016/B0-12-176480-X/00507-6.